Geophysical Journal International

Geophys. J. Int. (2013) **193,** 437–451 doi: 10.1093/gji/ggs131

Probabilistic full waveform inversion based on tectonic regionalization—development and application to the Australian upper mantle

Paul Käufl,[1] Andreas Fichtner[1] and Heiner Igel[2]

[1]*Department of Earth Sciences, Utrecht University, Utrecht, the Netherlands. E-mail: p.j.kaufl@uu.nl*
[2]*Department of Earth and Environmental Sciences, Geophysics Ludwig-Maximilian University, Munich, Germany*

Accepted 2012 December 30. Received 2012 December 8; in original form 2012 May 11

SUMMARY

We present a first study to investigate the feasibility of a probabilistic 3-D full waveform inversion based on spectral-element simulations of seismic wave propagation and Monte Carlo exploration of the model space. Through a tectonic regionalization we reduce the dimension of the model space to 12, and we incorporate complete seismograms in order to exploit all available information in the period range from 60 to 200 s.

S-wave velocity variations in the Australian Archean and Proterozoic lithospheres are generally well-constrained and strongly positive, in agreement with previous inferences from deterministic tomography. The maximum likelihood model reveals significantly elevated *P* velocities. While consistent with body wave studies, they are, however, not well constrained by our data, thereby providing an interesting example of a comparatively insignificant maximum-likelihood model.

Our data are notably affected by 3-D density variations. The effect, however, appears to be misleading. Both the maximum-likelihood model and the posterior probability densities strongly prefer unrealistically large positive density variations that are inconsistent with independent information from geodynamics and mineral physics. This suggests that highly probable and less extreme density models may be hidden in small and hardly detectable subvolumes of the 12-D model space. It follows that deterministic full waveform inversions for density may require particularly accurate initial models.

From a methodological perspective we must conclude that a transition to significantly higher dimensions would currently be difficult. Available computing power clearly imposes restrictions. However, even when Moore's law continues to hold, the largest obstacle appears to be our inability to efficiently map small high-dimensional subvolumes with high probability.

Key words: Inverse theory; Probability distributions; Seismic tomography; Australia.

1 INTRODUCTION

1.1 State of the art

Advances in computational seismology allow us to model the propagation of seismic waves through heterogeneous earth models with high accuracy, and to exploit information from complete seismograms for the benefit of improved tomographic images (e.g. Chen *et al.* 2007; Tape *et al.* 2009; Fichtner *et al.* 2010a; Lekic & Romanowicz 2011). The size of such modern full waveform inversions typically requires their formulation in terms of a deterministic misfit minimization problem that is solved iteratively with gradient-type methods. While being efficient from the pure minimization perspective, these deterministic inversions suffer from several drawbacks: Gradient methods may converge to potentially meaningless local minima, unless the initial model is sufficiently close to the global minimum. This deficiency results from the inherently non-linear relation between seismic data and 3-D Earth structure, and has been well documented since the early days of full waveform inversion (e.g. Gauthier *et al.* 1986). Furthermore, deterministic solutions to non-linear inverse problems do not provide information on model uncertainties. Tools from linear resolution analysis, including for instance the null-space shuttle (Deal & Nolet 1996; de Wit *et al.* 2012) or matrix probing (An 2012; Trampert *et al.* 2012), do not reflect the full range of models compatible with the data when the likelihood is related non-linearly to the model parameters. Therefore, synthetic inversions of chequer board patterns are mostly used as rough estimators of resolution, despite their well-known potential to be insignificant and misleading (Lévêque *et al.* 1993). Resolution analyses based on approximations of the Hessian

provide more complete information on uncertainties and trade-offs, but still refer to a specific minimum of the misfit function (Fichtner & Trampert 2011a,b).

Probabilistic inversions on the basis of Bayes' theorem and model space sampling, give access to the full posterior probability distribution that captures all available information on model parameters, including uncertainties (e.g. Resovsky & Trampert 2003; Trampert *et al.* 2004; Meier *et al.* 2007a). Furthermore, model space sampling is able to explore the possibly non-linear function relating the model space to the data space, without locking into local minima.

While often being considered the most elegant and general formulation of an inverse problem (Tarantola 2005), the probabilistic approach suffers from the diverse facets of the curse of dimensionality, that is, the difficulty to sample a high-dimensional model space efficiently and to infer useful information from the resulting ensemble of test models (e.g. Backus 1988; Curtis & Lomax 2001; Jackson & Sambridge 2005). Therefore, strong restrictions apply to the size of the model space.

An efficient approach to model space reduction is based on tectonic regionalizations. Instead of using quasi-exhaustive parametrizations in terms of blocks, spherical harmonics or wavelets, a small number of basis functions is defined from prior knowledge of large-scale tectonic features with nearly homogeneous distributions of seismic properties. While popular since the early days of seismic tomography (e.g. Kanamori 1970; Dziewonski & Steim 1982) tectonic regionalizations have so far not been discovered as a vehicle towards probabilistic full waveform inversion, despite their potential to reveal model uncertainties and to test tangible geologic hypotheses.

1.2 Objectives of this work

The present study constitutes a first experiment on our way towards 3-D probabilistic full waveform inversion. Our objectives are therefore comparatively modest, and of both technical and geologic nature.

From a purely technical point of view, we explore the feasibility of a full waveform inversion based on spectral-element simulations of seismic wave propagation, tectonic regionalization and model space sampling via the Neighbourhood Algorithm (Sambridge 1999a,b). Specific questions that we address concern the tractable number of model space dimensions, the convergence of the sampling algorithm and the interpretation of the multidimensional posterior probability density.

The target region of our experiment is the Australian continent. The analysis of the posterior probability density therefore provides insight into various aspects of Australian Earth structure. These include (1) the robustness of unusually high velocities within the Archean Pilbara and Yilgarn cratons (see figures 1 and 2), and (2) the likelihood of anomalously low velocities beneath the central Australian Proterozoic provinces found in recent tomographic studies (Fishwick & Reading 2008; Fichtner *et al.* 2010a) and attributed to perturbations of the thermal regime or an increased Cr concentration.

Model space sampling provides a natural solution to multiparameter inverse problems that are difficult to handle in deterministic inversions due to potentially complex trade-offs between model parameters. More specifically, probabilistic inversion allows us to address the possibility of resolving 3-D density variations that are typically ignored or scaled to velocity variations in traditional traveltime and surface wave tomography. Evidence that full waveform inversion provides purely elastic, that is, non-gravitational, constraints on density heterogeneities is accumulating (Y. Capdeville, personal communication, 2008; Köhn *et al.* 2010; Jeong *et al.* 2012), but the full potential remains to be explored.

1.3 Outline

This article is organized as follows. In Section 2, we briefly review the large-scale geologic setting of Australia in the context of recent tomographic studies, and we describe the tectonic regionalization that enables the construction of random test models. Following a summary of the seismic data set in Section 3, Section 4 provides details concerning the probabilistic inversion, including the choice of prior information and the solution of the forward problem using spectral-element simulations. Results of the inversion procedure in the form of the maximum-likelihood model, 1-D and 2-D marginals are presented in Section 5. Finally, we discuss problems that need to be resolved before making the transition to larger-scale full waveform inversions (Section 6).

2 MODEL CONSTRUCTION AND PARAMETRIZATION

2.1 Geologic setting and tectonic regionalization

The tectonic regionalization is based on the clear identification of two large-scale ($\gtrapprox$1500 km) structural elements in continental Australia: the Archean cratons in the west and the predominantly Proterozoic units in the centre (Fig. 1). Both Archean and Proterozoic lithospheres have been imaged consistently in several recent surface wave tomographic studies (Debayle & Kennett 2000; Yoshizawa & Kennett 2004; Fishwick *et al.* 2005; Fishwick & Reading 2008; Fichtner *et al.* 2010a,b) and are key components of the Australian Seismological Reference Model (AuSREM, Kennett *et al.* 2013). Significant differences between the tomographic images are limited to length scales below about 1500 km (Fichtner *et al.* 2012).

Archean Australia is composed of the Pilbara and Yilgarn cratons that joined during the Early-Proterozoic Capricorn orogeny (Myers *et al.* 1996). In tomographic images, the Archean lithosphere is marked by anomalously high S velocities, reaching $+8$ per cent with respect to the radial average on a 1500 km length scale (Fig. 2). On length scales around 500 km, S velocity variations of up to $+12$ per cent can be observed (e.g. Fichtner *et al.* 2010a), therefore questioning a purely thermal interpretation (see also Section 6.5).

The central part of the Australian continent is predominantly Proterozoic, the only exception being the Archean Gawler craton in South Australia. The Tasman Line is the boundary between Proterozoic units and the Phanerozoic Delamerian, Lachlan and New England fold belts in eastern and southeastern Australia. Its near-surface location inferred from outcrops and gravity and magnetic measurements (Wellman 1998) is further west than its location at greater depth as seen in tomographic images (e.g. Zielhuis & van der Hilst 1996) and isotopic studies (Handler *et al.* 1997). Proterozoic Australia has remained tectonically stable since the Mid-Palaeozoic Alice Springs orogeny (400–300 Ma). The elastic properties of the Proterozoic lithosphere are strongly depth-dependent with a structural boundary located around 150 km depth. In the uppermost 150 km, seismic velocities are only slightly higher than the radial average and the pattern of azimuthal anisotropy is complex. Between 150 km depth and the base of the lithosphere, velocities are as high as in the Archean and the azimuthal anisotropy is coherently

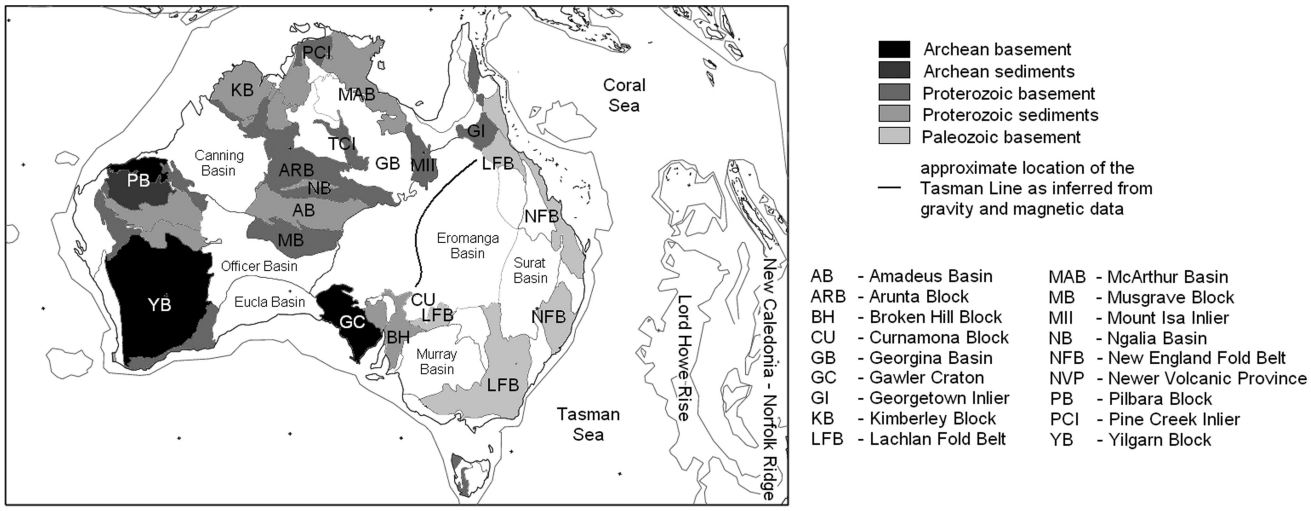

Figure 1. Map of major surface-geological features in the study area. Adapted from Myers *et al.* (1996).

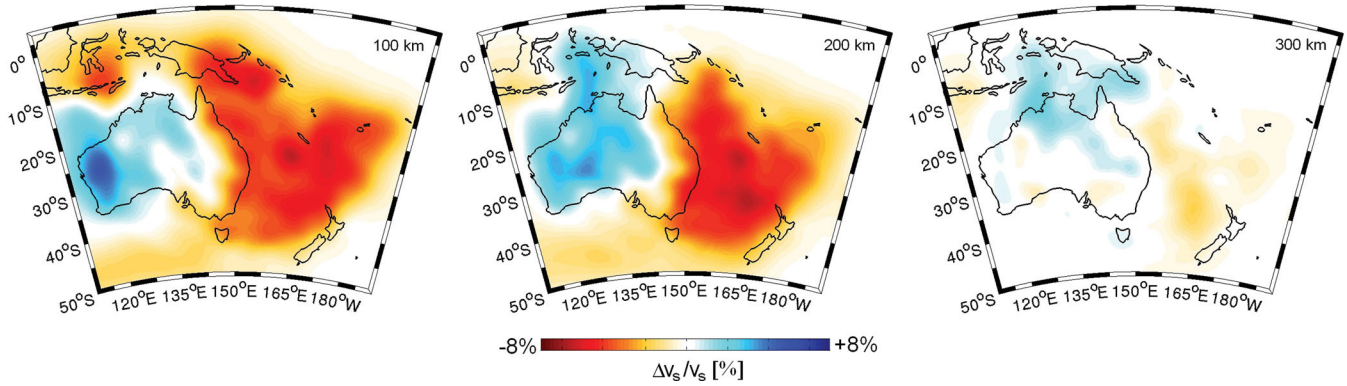

Figure 2. *S* velocity distribution in the Australian upper mantle inferred from full waveform inversion (Fichtner *et al.* 2010a). To allow a comparison with the results of this study (Fig. 9) the original tomographic images were filtered to suppress wavelengths shorter than ∼1800 km. Details of the filtering process and filter characteristics are given in Appendix A. Precambrian Australia is clearly distinguished by higher than average velocities. Above 150 km depth, the *S* velocity in the Archean Pilbara and Yilgarn cratons is ∼4 per cent higher than in the Proterozoic regions of central Australia.

related to the direction of absolute plate motion (Debayle & Kennett 2000; Simons *et al.* 2002; Fishwick & Reading 2008). The depths of the Archean and Proterozoic lithospheres estimated from surface wave tomography are 230 ± 30 km, depending on the method and data used.

The clear division of Precambrian Australia both laterally and in depth suggests the definition of two principal tectonic regions: the Archean and the Proterozoic lithospheres, each with depth-dependent properties.

2.2 The construction of test models

Based on the previous considerations we construct earth models $m(\mathbf{x})$ as filtered superpositions of weighted basis functions $b_i(\mathbf{x})$ defined by the tectonic regions, that is,

$$\delta\tilde{m}(\mathbf{x}) = \delta m_0(\mathbf{x}) + \sum_{i=1}^{N} \delta m_i \, b_i(\mathbf{x}), \tag{1a}$$

$$\delta m(\mathbf{x}) = (F * \delta\tilde{m})(\mathbf{x}), \tag{1b}$$

$$m(\mathbf{x}) = \delta m(\mathbf{x}) + m_{bg}(z), \tag{1c}$$

where $\delta m(\mathbf{x})$ is a perturbation of either the *S* velocity, δv_s, the *P* velocity, δv_p, or density, $\delta\rho$ with respect to a 1-D background model $m_{bg}(z)$. Motivated by the large-scale tectonic setup of the Australian continent, described in Section 2.1, we define the following four basis functions, visualized in Fig. 3: b_1 and b_2 comprise the Archean lithosphere from 0 to 150 km depth and from 150 to 230 km depth, respectively; b_3 and b_4 represent the Proterozoic lithosphere in the same depth intervals. The small number of basis functions results from the absence of more than two coherent large-scale (>1500 km) tectonic provinces, and from the requirement of a small model space dimension in probabilistic inversions. Structure outside the basis functions is accounted for by the contribution $\delta m_0(\mathbf{x})$ in eq. (1a). In our models, $\delta m_0(\mathbf{x})$ comprises the Phanerozoic continental lithosphere in eastern Australia and the oceanic lithosphere and upper mantle surrounding the continent.

Following the superposition of the basis functions with variable scaling factors δm_i, we apply a spatial filter F, symbolized by eq. (1b). The filter acts as a lowpass, and it serves two purposes: (1) It prevents the occurrence of unrealistically strong guided waves along the sharp boundaries of the basis functions and (2) it reduces the influence of errors in the locations of the object boundaries. Details of the spatial filtering are given in Appendix A and in Fichtner

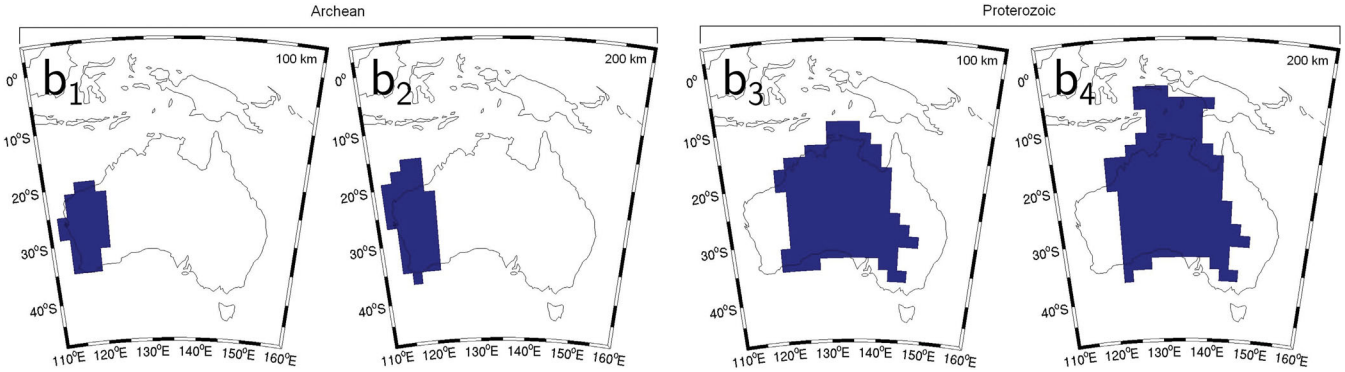

Figure 3. Left-hand side: horizontal slices through the basis functions b_1 and b_2 for Archean lithosphere. Right-hand side: horizontal slices through the basis function b_3 and b_4 for Proterozoic lithosphere.

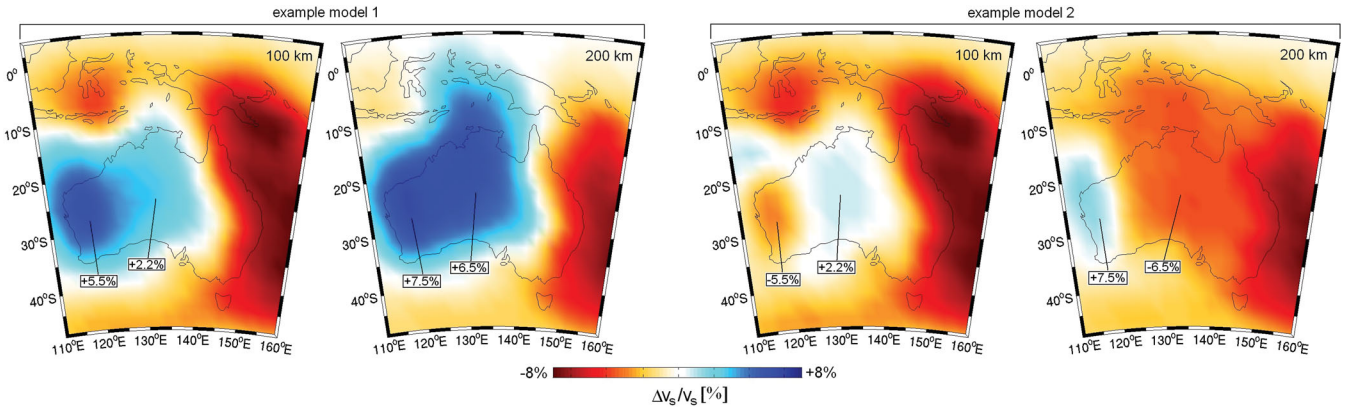

Figure 4. Horizontal slices through the *S* velocity distributions of two test models at 100 and 200 km depth. The peak velocity perturbations in the Archean and Proterozoic lithospheres at the different depth levels are indicated in the images. As a result of the spatial filtering process, the average perturbations are ∼20 per cent smaller than the peak perturbations.

Table 1. Overview of the 12 independent model parameters.

Parameter		Related basis function
S-wave speed perturbations	δv_{s1}	b_1, Archean, top layer
	δv_{s2}	b_2, Archean, bottom layer
	δv_{s3}	b_3, Proterozoic, top layer
	δv_{s4}	b_4, Proterozoic, bottom layer
P wave speed perturbations	δv_{p1}	b_1, Archean, top layer
	δv_{p2}	b_2, Archean, bottom layer
	δv_{p3}	b_3, Proterozoic, top layer
	δv_{p4}	b_4, Proterozoic, bottom layer
Density perturbations	$\delta \rho_1$	b_1, Archean, top layer
	$\delta \rho_2$	b_2, Archean, bottom layer
	$\delta \rho_3$	b_3, Proterozoic, top layer
	$\delta \rho_4$	b_4, Proterozoic, bottom layer

et al. (2012). The lowpass filtering entails a ∼20 per cent reduction of the peak heterogeneities that must be taken into account in the interpretation stage. Fig. 4 shows the *S* velocity distributions of two test models at 100 and 200 km depth, respectively.

The parametrization introduced above defines a 3-D model in terms of 12 scalar parameters (see Table 1): perturbations of the *P* velocity δv_p, the *S* velocity δv_s and density $\delta \rho$ with respect to a modified version of the 1-D, isotropic PREM (Dziewonski & Anderson 1981, Fig. 5), within each of the four basis functions. The actual earth model $m(\mathbf{x})$ used for the forward calculations is thus retrieved by adding the 1-D background model $m_{bg}(z)$ to the 3-D perturbation model $\delta m(\mathbf{x})$ (eq. 1c). Thus, our goal is to compute the posterior probability distribution in a 12-D model space.

3 DATA

We selected seismic waveform data that are primarily sensitive to the regions covered by the four basis functions defined in the previous section. Furthermore, we applied the following data selection criteria: (1) The signal-to-noise ratio in the period range from 50 to 200 s must exceed 20. (2) The surface wave magnitude of the events must not exceed 6.9 to avoid the need to model finite source effects. Our final data set comprises 338 seismograms, originating from 10 shallow events that occurred along the plate boundaries north of Australia. The data were recorded at 30 stations operated by The Australian National University, Geoscience Australia, GEOSCOPE, IRIS/IDA and IRIS/USGS. The ray coverage is shown in Fig. 6.

In the interest of simplicity, we only analysed vertical-component seismograms that do not require polarization anisotropy. From the raw data we produced two data subsets by bandpass filtering between 60 and 200 s, as well as between 130 and 200 s. The filtered seismograms used in the inversion mostly contain fundamental- and higher-mode surface waves but also long-period body waves and unidentified waveforms. Simultaneously inverting data in two

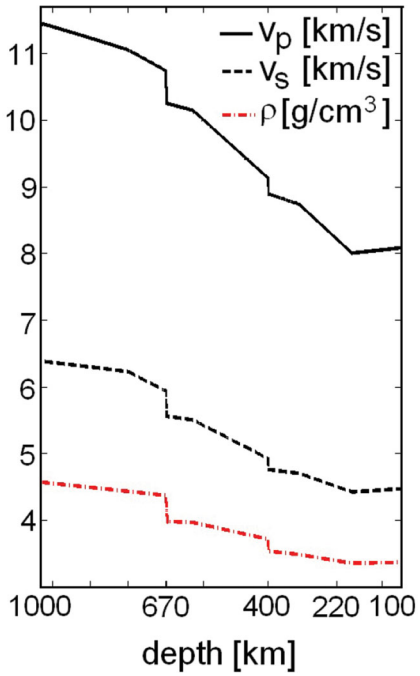

Figure 5. The 1-D background model is a modified version of the isotropic PREM (Dziewonski & Anderson 1981), where the discontinuity at 220 km depth has been replaced by a linear gradient.

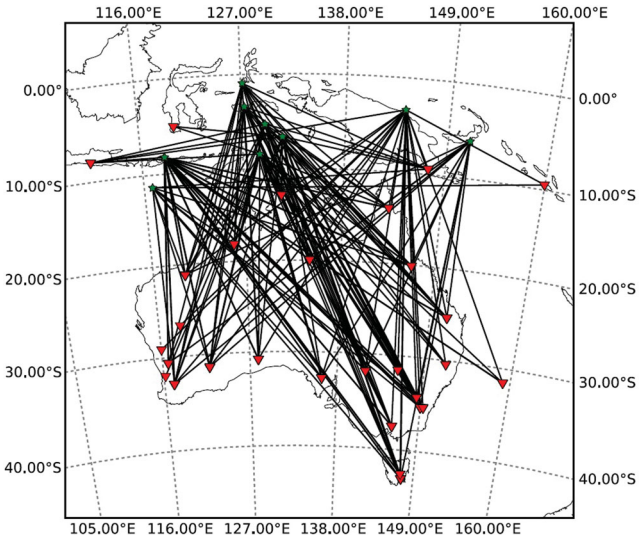

Figure 6. Ray coverage for the 338 vertical-component recordings in the data set. Stations and epicentres are marked by red triangles and green stars, respectively.

different period ranges is intended to enhance depth resolution. Rayleigh wave sensitivity shows a peak at around 50 km depth for a period of 60 s and at around 150 km depth for a period of 130 s (Takeuchi & Saito 1972). Based on the shape of surface wave sensitivity kernels, we therefore expect the data to resolve upper-mantle structure to a depth of ∼250 km. However, the ray coverage shown in Fig. 6 indicates that the central Australian Proterozoic is likely to be better constrained than the Archean in Western Australia. The choice to work with comparatively long-period waveforms is motivated by the need to keep the computational costs of 3-D numerical wave propagation at an acceptable level.

4 PROBABILISTIC INVERSION USING THE NEIGHBOURHOOD ALGORITHM

In the following paragraphs we describe the technical details of the inverse problem, including its Bayesian formulation, the choice of prior information, the construction of a suitable misfit measure and the solution of the forward problem. We assume that the uncertainties in the forward simulations are negligible compared to the errors in the observed data. Invoking Bayes' theorem, the posterior probability density can then be written as (e.g. Tarantola 2005)

$$\sigma(\boldsymbol{m}|\boldsymbol{d}) = \frac{1}{\nu}\rho_M(\boldsymbol{m})L(\boldsymbol{m}|\boldsymbol{d}), \tag{2}$$

where $\boldsymbol{m} \in \mathbb{M}$ denotes an element of the 12-D model space, $\rho_M(\boldsymbol{m})$ is the prior probability density in the model space, and $L(\boldsymbol{m}|\boldsymbol{d})$ denotes the likelihood of model $\boldsymbol{m}$ given data $\boldsymbol{d}$. The normalization constant ν is determined by $\nu = \int_{\mathbb{M}} \rho_M(\boldsymbol{m})L(\boldsymbol{m} \mid \boldsymbol{d})\, d\boldsymbol{m}$. The Bayesian approach requires us to choose the form of the likelihood function as well as the prior distribution in advance.

4.1 Prior information

The choice of the prior distribution ρ_M is to some degree subjective, and therefore often considered to be a weak point of Bayesian inference. This subjectivity, however, is well acceptable when we admit that any inference is relative to the prior—meaning that the interpretation of our inferences must account for the choice of subjective prior information (Jaynes 2003).

Since there are no generally accepted rules for the construction of prior distributions, we adopt a pragmatic approach, the consequences of which are discussed in detail in Section 6. First, we note that most tomographic studies of the Australian continent revealed higher than average velocities within both the Archean and Proterozoic, at least over length scales larger than ∼1500 km. We therefore choose the prior distributions of the P and S velocity perturbations to be constant within and zero outside the following intervals:

$$\delta v_s \in [0, 0.6] \text{ km s}^{-1}, \tag{3}$$

$$\delta v_p \in [0, 0.8] \text{ km s}^{-1}. \tag{4}$$

The upper limits of these intervals are chosen to be well above previously reported values. Rough bounds on plausible density variations can in principle be deduced from gravity and mineral physics data. However, we deliberately ignore these sources of information in order to isolate the constraints on density from seismic data alone. Therefore, we also choose a constant prior for ρ within the interval

$$\delta\rho \in [-0.4, 0.4] \text{ g cm}^{-3}. \tag{5}$$

We expect this interval to be sufficiently broad, because density variations beyond ± 0.4 g cm^{-3} would be highly unlikely given the long-term gravitational stability of the Australian continent and gravity observations (e.g. Reigber *et al.* 2007).

While the prior distributions are formally constant and independent, the spatial filtering in the construction of test models (Section 2.2) effectively leads to position-dependent Gaussian-like priors with mutual correlations. These are shown in Fig. 10 for the central point of each basis function. The modification of the originally constant and independent priors reflects our decision to enforce continuity and similar correlation lengths throughout the test models. The filtering process introduces the strongest correlations for basis functions with a smaller volume, thereby naturally equilibrating the

effective number of free parameters in relation to the volume of a basis function. These effects will be accounted for in the interpretation stage (Section 5.2).

4.2 Misfit functional design

The design of suitable misfit functionals for full waveform inversion is the subject of ongoing research (e.g. Crase *et al.* 1990; Gee & Jordan 1992; Fichtner *et al.* 2008; Brossier *et al.* 2010; Bozdağ *et al.* 2011; Rickers *et al.* 2012); and the optimal choice is likely to be strongly problem-dependent. Our misfit functional is intended to extract as much information as possible while being robust and largely insensitive to absolute amplitudes that often cannot be measured reliably.

We denote by $u_0(\mathbf{x}_s, \mathbf{x}_r, t)$ and $u(\mathbf{x}_s, \mathbf{x}_r, t)$ the filtered versions of the observed and synthetic vertical-component seismograms, with source position $\mathbf{x}_s$ and receiver position $\mathbf{x}_r$. As a measure for the discrepancy between observed and synthetic seismograms we choose the L_1-normalized difference

$$\phi(\mathbf{x_s}, \mathbf{x_r}, t) = \frac{u_0(\mathbf{x}_s, \mathbf{x}_r, t)}{||u_0(\mathbf{x}_s, \mathbf{x}_r)||_1} - \frac{u(\mathbf{x}_s, \mathbf{x}_r, t; \mathbf{m})}{||u(\mathbf{x}_s, \mathbf{x}_r; \mathbf{m})||_1}. \quad (6)$$

The cumulative misfit χ is then defined as the weighted sum of the L_1 distances between the individual L_1-normalized waveforms

$$\chi_T(\mathbf{m}) = \sum_r w_r \sum_s \left|\left| \frac{u_0(\mathbf{x}_s, \mathbf{x}_r)}{||u_0(\mathbf{x}_s, \mathbf{x}_r)||_1} - \frac{u(\mathbf{x}_s, \mathbf{x}_r; \mathbf{m})}{||u(\mathbf{x}_s, \mathbf{x}_r; \mathbf{m})||_1} \right|\right|_1, \quad (7)$$

where T denotes the period range from 60 to 200 s and 130 to 200 s, respectively. The weights w_r are chosen to compensate for the heterogeneous station distribution, shown in Fig. 6. This misfit definition has several advantages in the context of a probabilistic waveform inversion. Most importantly, the normalization of u_0 and u avoids the dominance of large-amplitude seismograms, recorded, for instance, at short epicentral distances. The misfit is, furthermore, robust, resistant against imprecise magnitude estimates, and unaffected by potentially erroneous instrument calibrations. A natural choice for the likelihood function in the case of an L_1 norm is the exponential distribution

$$L(\boldsymbol{m}) = c \exp\left[-\left(\frac{\chi_{60}(\mathbf{m})}{\sigma_{60}} + \frac{\chi_{130}(\mathbf{m})}{\sigma_{130}} \right) \right], \quad (8)$$

where c is a normalization constant, and σ_{60} and σ_{130} are frequency-dependent noise levels (see Section 6.2 for details).

4.3 Forward problem solution

To accurately account for the presence of strong 3-D heterogeneity, we simulate seismic wave propagation in a spherical section of the Earth using a spectral element method (Fichtner *et al.* 2010a). The computational domain ranges from 7.5°N to 50°S latitude, from 105°E to 160°E longitude and from the surface of the Earth to 1461 km depth. The domain is discretized using a total number of $36 \times 35 \times 20 = 25200$ hexahedral elements, within which the dynamic fields are approximated by 4th-order Lagrange polynomials collocated at the Gauss–Lobatto–Legendre points. With the rule of thumb that two elements per minimum wavelength are required to achieve acceptable accuracy, we are able to propagate waves with a minimum period of ∼60 s. The time-integration is based on a finite-difference approximation, and 4500 time steps of 0.3 s are calculated per event. The simulations were carried out in parallel on 120 processors using the TETHYS Linux cluster (Oeser *et al.* 2006) and the German national supercomputer HLRB2 at the Leibniz-Rechenzentrum München. The total computation time amounts to approximately 200 000 CPU hours on 1.6 GHz Intel Itanium2 processors with up to 6.4 GFlop/s per core.

4.4 Model space sampling

Random models are created as follows: We draw a random set of 12 parameter perturbations δm_i from the prior distribution, described in Section 4.1. From this set of perturbations we construct a 3-D earth model $\mathbf{m}(\mathbf{x})$ using equations 1a to 1c.

To sample the model space efficiently, we employed the Neighbourhood Algorithm, introduced by Sambridge (1999a,b). The algorithm is based on a piecewise constant approximation of the posterior probability density (eq. 2) given by the Voronoi diagram of the set of models $P_i = \{\mathbf{m}_1, \ldots, \mathbf{m}_n\}$ at the ith iteration of the algorithm. We started with an initial ensemble of 400 models drawn from the prior. After each iteration, n_s new models were added to this set, and the approximation was updated. The n_s new models were generated via a uniform random walk from each of the n_r lowest-misfit models, where the walks were restricted to the Voronoi cells surrounding the models. Thus, in each of the n_r selected cells n_s/n_r new models were generated. Effectively, the two parameters n_s and n_r control the exploratory behaviour of the algorithm.

In the inversion we adjusted the control parameters manually, based on the inspection of the proposed sampling density for different choices of n_s and n_r. For the first five iterations, we set $n_s = 400$ and $n_r = 20$ which resulted in a rather exploratory behaviour. Starting with the sixth iteration, however, we set $n_s = 200$ and $n_r = 10$ in order to increase the convergence speed. This change was motivated by the fact, that the sampler started to produce values for a subset of the parameters in a very small region of the model space already, whereas for other parameters new values were still distributed over the whole model space.

5 RESULTS

5.1 Data fit and the maximum likelihood model

We stopped the Neighbourhood Algorithm after 18 iterations, because the ensemble misfit did not continue to decrease significantly, as illustrated in Fig. 7. Furthermore, the posterior 1-D and 2-D marginals shown in Figs 12 and 13 did not change noticeably during the last couple of iterations, suggesting that the Neighbourhood Algorithm had indeed converged. The final ensemble consists of 5000 models.

Fig. 8 shows four examples of waveforms generated from high- and low-likelihood models in the ensemble. For most stations, the high-likelihood model is able to reproduce the observed waveforms in detail. The few outliers (see right-hand column of Fig. 8) have a small effect on the misfit functional thanks to its robustness.

Horizontal slices through the maximum likelihood model, that is, the model with the best data fit, are shown in Fig. 9 for 100 and 200 km depth. The S velocity part agrees remarkably well with the long-wavelength variant of the model by Fichtner *et al.* (2010a), shown in Fig. 2. The only notable difference is the slightly reduced strength of the heterogeneities in our regionalized model, which most likely results from the averaging over the large volumes defined by the basis functions.

The P velocity part of the maximum likelihood model, shown in the central column of Fig. 9, reveals elevated P velocities of

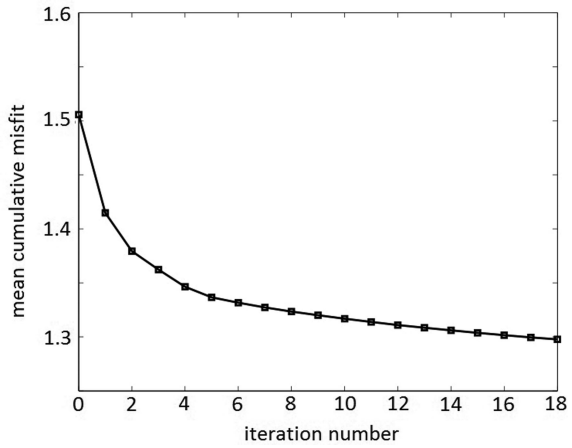

Figure 7. Mean cumulative misfit versus iteration number. The mean cumulative misfit of all models in the ensemble has been reduced significantly after 18 iterations, suggesting that the sampler has moved towards low-misfit areas.

~3 per cent throughout the central and western Australian lithospheres. This result is in accord with regional body wave studies that found large-scale positive *P* velocity anomalies of 2–3 per cent in the northern part of Precambrian Australia (Kaiho & Kennett 2000). The reliability of this result will be discussed in Section 5.2.

The third column of Fig. 9 displays the density part of the maximum likelihood model. The density perturbations preferred by the seismic data are generally positive, reaching values of 5–6 per cent. However, the absence of large-scale positive geoid anomalies (e.g. Reigber *et al.* 2007) and the long-term gravitational stability of the central and western Australian lithospheres suggests neutral or slightly negative density variations (Jordan 1975). Xenolith data typically imply negative density variations of around −2 per cent in the 100–200 km depth range beneath cratons (e.g. James *et al.* 2004). This discrepancy will be the subject of further discussions in the following paragraphs.

The primary motivation for a probabilitic inversion is the quantification of uncertainties and possible trade-offs between model parameters. We therefore analyse the posterior probability density

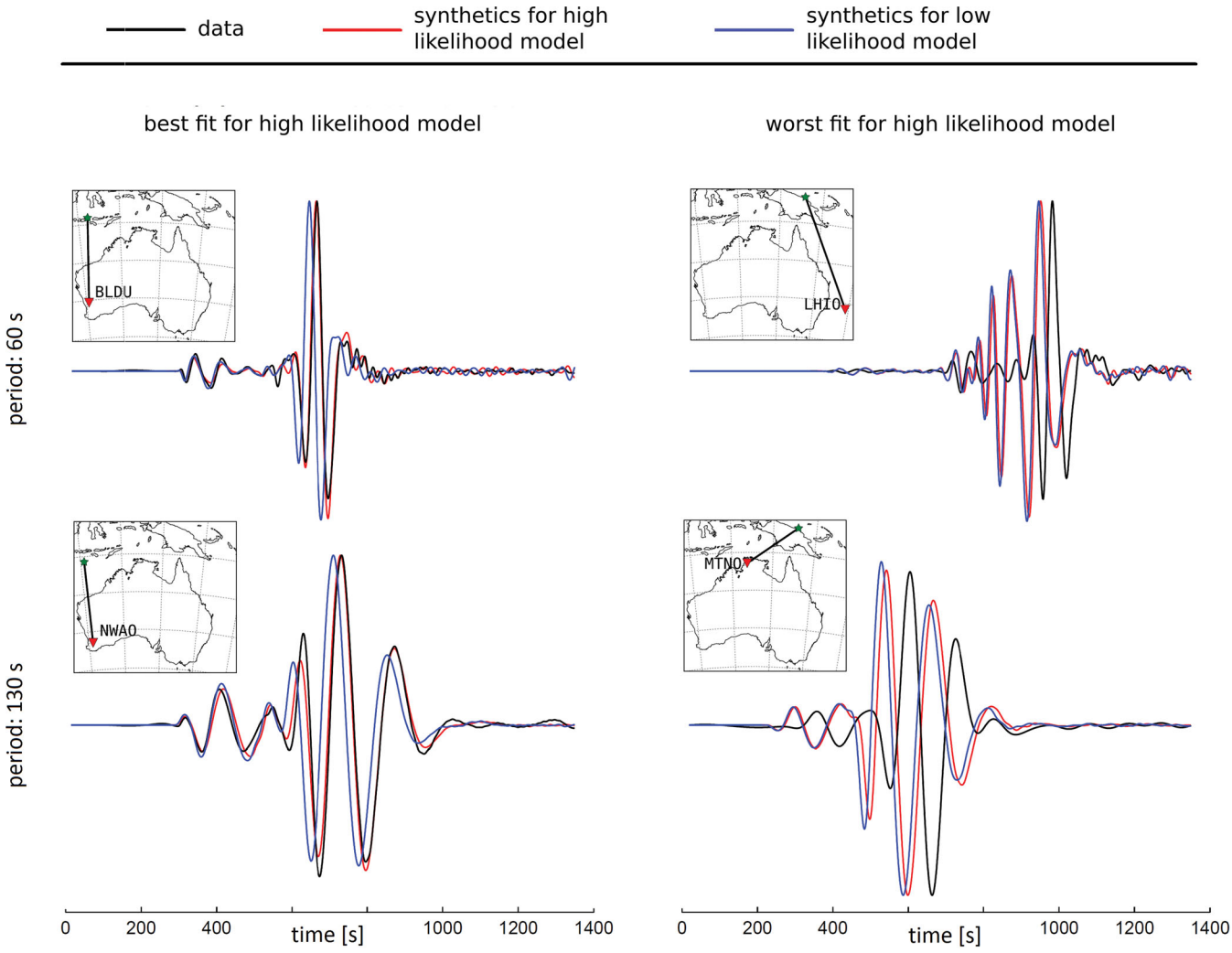

Figure 8. Observed waveforms (black) for different events and stations compared with synthetic seismograms generated using a low- (blue) and a high-likelihood (red) model from the ensemble. Left-hand panel: Recordings with the highest fit in the data set. Right-hand panel: Waveforms with the lowest fit in the data set.

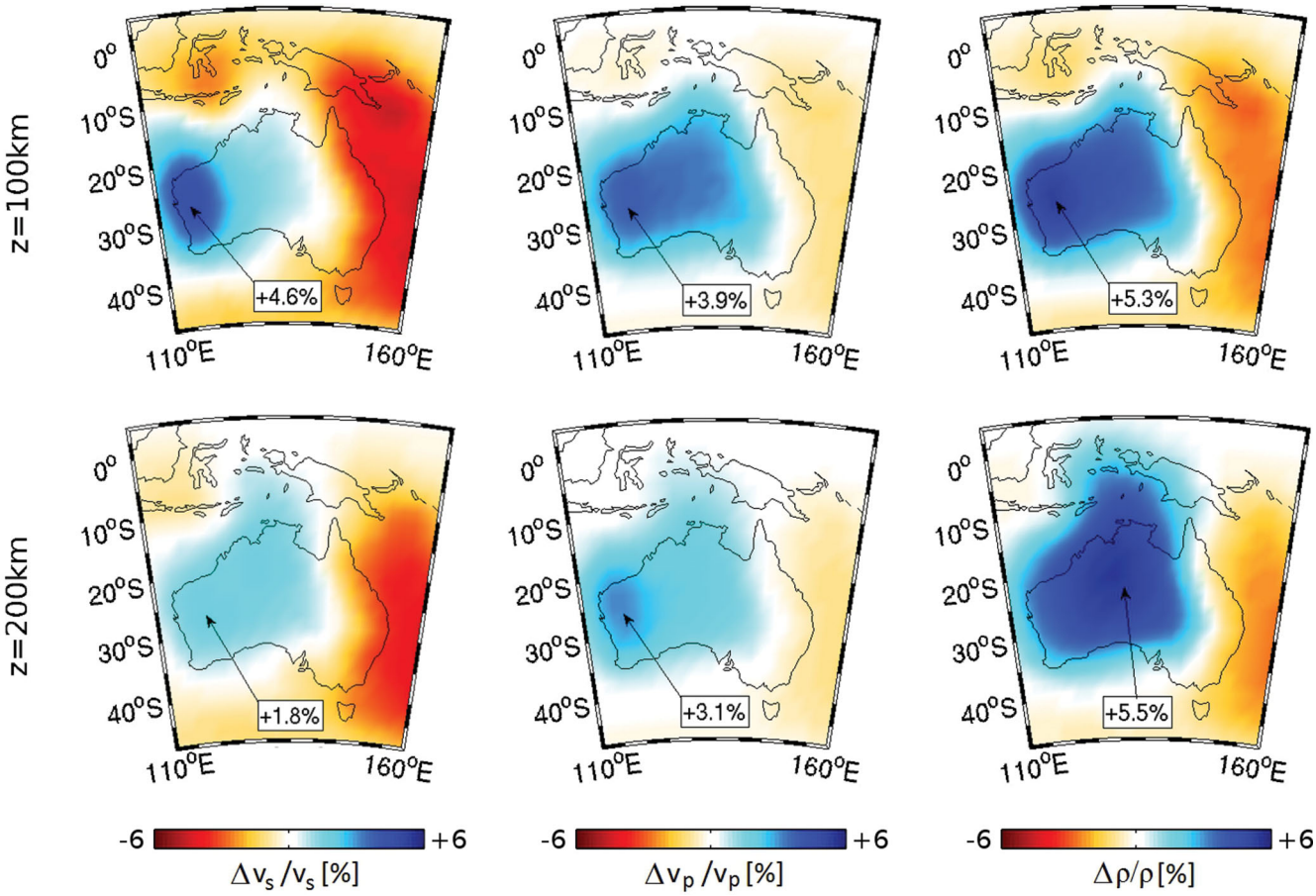

Figure 9. Horizontal slices through the maximum likelihood model at 100 and 200 km depth, respectively. While the *S* and *P* velocity variations agree well with deterministic surface wave tomographies and body wave studies (e.g. Kaiho & Kennett 2000; Fichtner *et al.* 2010a), the density variations are significantly larger than those inferred from independent geodynamic and mineral-physics observations.

in the following section. This will also provide more insight into the nature of the high densities of the maximum likelihood model.

5.2 Analysis of the posterior distribution

The final ensemble of 5000 test models provides an approximation of the joint posterior probability density (see Section 4). We create samples of the posterior by resampling the ensemble using the Neighbourhood Algorithm (Sambridge 1999b). We subsequently obtain marginal distributions from the resampled ensemble by Monte Carlo integration as described in Sambridge (1999b). We show results for two different choices for the noise level σ of eq. (8), a less conservative estimate, with $\sigma_{60} = 0.4 \times 10^{-3}$, $\sigma_{130} = 1.7 \times 10^{-3}$, and a more conservative estimate with $\sigma_{60} = 1.6 \times 10^{-3}$, $\sigma_{130} = 7.3 \times 10^{-3}$.

To account for the influence of the spatial filter used in the construction of test models, we convolve models drawn from the prior and the posterior with the spatial filter given in equation (1). This provides position-dependent priors and posteriors, which we evaluate at the central point of each basis function, defined as

$$\mathbf{r}_i^c = \frac{1}{V_i} \int_{V_i} \mathbf{r} \mathrm{d}V, \tag{9}$$

where v_i is the volume of the ith basis function. Note that the central points approximately coincide with the points indicated by arrows in Fig. 9. Results are given in Fig. 10 for the less conservative and in Fig. 11 for the more conservative noise estimate.

We observe different classes of posterior marginals: Most distributions are unimodal. They show either a pronounced peak well within the sampling interval, or they resemble the prior distribution. In some cases, however, a pronounced peak aligns with the edge of the prior range (e.g. Proterozoic top *S* wave speed and Proterozoic bottom density in Fig. 10).

The *S* velocity is generally well constrained. This is expected because our comparatively long-period waveforms (dominantly Rayleigh waves) are mostly sensitive to *S* velocity perturbations. The second row of Fig. 10 suggests, that there is also limited information on the *P* velocities. However, a comparison with Fig. 11 reveals, that the information is comparatively weak, and in fact vanishes upon increasing of the noise level towards the more conservative estimate. This result is expected because of the almost negligible sensitivity of long-period waveforms to *P* velocity perturbations. It follows that the maximum likelihood *P* velocity model—while plausible and consistent with body wave studies—is not necessarily significant. *P* velocity variations cannot be constrained well with our data.

Two of the density marginals (Archean bottom, Proterozoic top) rather closely resemble the prior, suggesting only limited information on these parameters is present. In the Archean top and Proterozoic bottom layers, however, they show very pronounced peaks. These marginals appear suspicious, because a significant part of the probability mass lies in regions where the prior nearly vanishes.

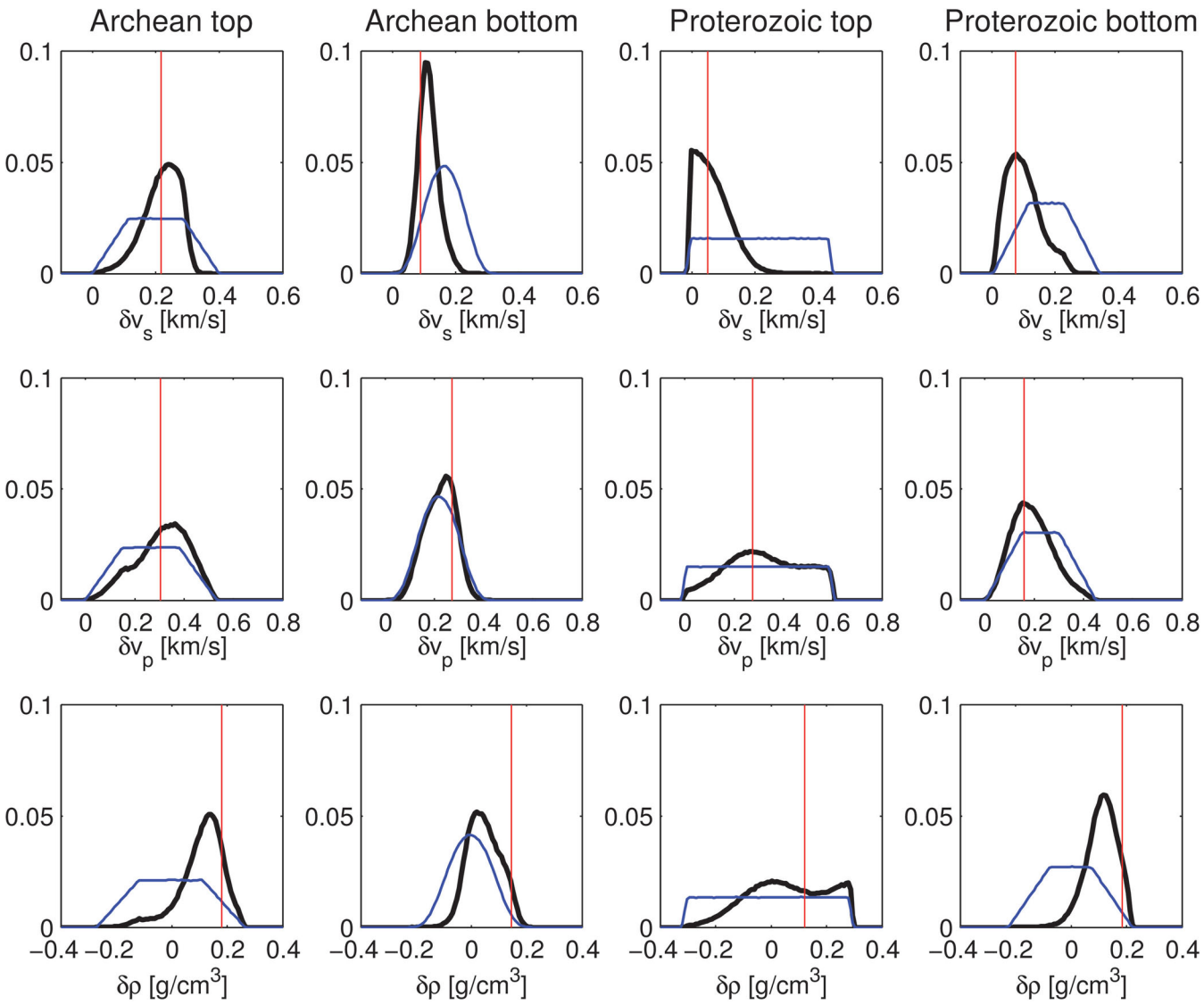

Figure 10. Prior (blue) and posterior (black) marginals evaluated at the central point in each of the four objects (eq. 9) for a comparatively low noise level σ. Note that the spatial filtering of the test models leads to more Gaussian-type priors that differ from the originally constant priors (eqs 3–5) depending on the size of the corresponding basis function. The red vertical lines indicate the position of the maximum likelihood model shown in Fig. 9.

To further investigate this issue, we consider the unfiltered posterior distributions in Fig. 12. They serve as an additional diagnostic tool that does not suffer from the subjectivity in choosing a specific location within the basis functions. Also in the unfiltered posteriors for density a strong peak lies at the edge of the model space. One might argue that this is also the case for the bottom layer *S* velocity distributions. However, the actual marginals for *S* velocity show a pronounced peak lying within the range of *a priori* plausible models. The density marginals, in contrast, suggest that prior assumptions were wrong and strongly positive density variations may in fact be well constrained by the seismic data.

There are two possibilities to reconcile this result with geodynamic and mineral-physics constraints: First, there may be trade-offs in the form of simultaneous variations of two or more parameters that compensate each other such that the misfit remains largely unchanged. In this case, the high-density models may be insignificant. Second, the Neighbourhood Algorithm may have missed models with lower density and low misfit, possibly because they occupy a relatively small volume in model space.

To assess the existence of trade-offs, we analyse 2-D posterior marginal distributions that describe the effect of simultaneous variations of two model parameters. A collection of density–density as well as several velocity–density marginals is shown in Fig. 13. These 2-D marginals do not suggest the existence of any significant trade-offs between density parameters themselves or between densities and velocities. However, 2-D marginals are, in general, only an integral summary of a higher-dimensional probability distribution—meaning that their diagnostic capabilities are limited. Pronounced trade-offs may be hidden in small volumes of the model space, therefore getting lost during the integration process. The severity of this effect increases very rapidly with increasing model space dimension (Curtis & Lomax 2001); and 12 dimensions may already be critical given the data in our study. Furthermore, significant trade-offs may exist in model subspaces with more than two dimensions. This would make their detection almost impossible because the human visual analysis tools are essentially limited to 2-D. In summary, we cannot exclude the existence of trade-offs that may render excessively high densities insignificant.

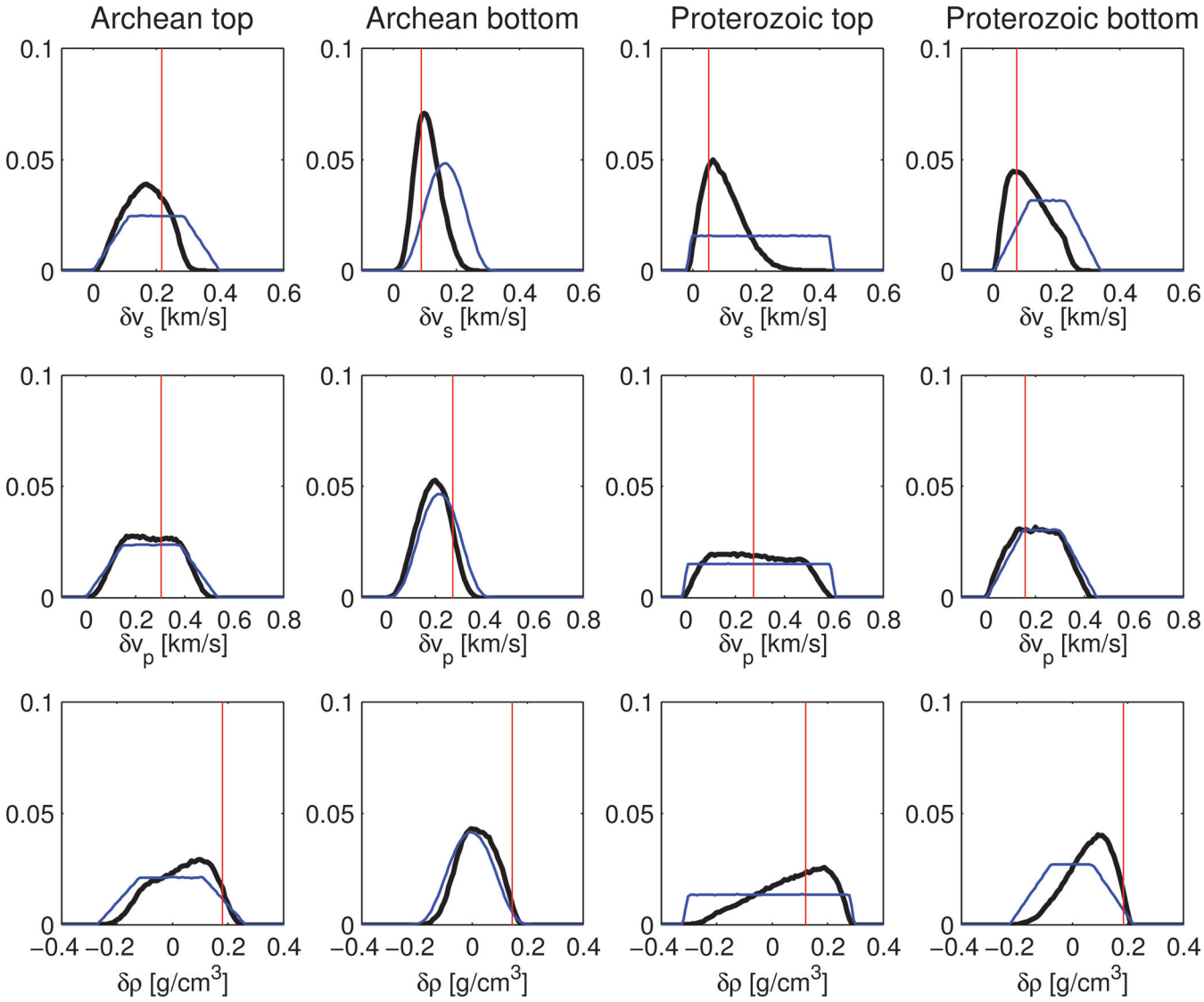

Figure 11. Same as Fig. 10, but for a more conservative noise level σ. Note that all distributions are less pronounced and that the posterior *P*-wave velocity distributions now closely resemble the according priors, indicating that the information on these parameters is comparatively weak.

The option that the sampler missed lower-density models with low misfit also cannot be excluded, despite the apparent convergence of the Neighbourhood Algorithm that manifests itself, for instance, in the convergence of the posterior marginals (Fig. 7). When the models with the lowest misfits are confined to a small volume in model space, they become almost impossible to detect with a finite number of samples. This problem is a particular facet of the curse of dimensionality that strongly limits the information contained in posterior distributions that are approximated by sampling: Good models can certainly be found in regions of high probability, but there may be better models hidden in small subvolumes within broad regions of low probability.

6 DISCUSSION

6.1 Choice of the prior

The choice of prior information is inherently subjective, and it strongly affects the posterior, especially when constraints from data are weak. Suggestions for the construction of prior distributions, including for instance Jeffrey's and maximum-entropy priors, are not based on universal principles and merely transfer subjectivity to a higher level.

Our decision to use constant priors over broad intervals was intended to make the constraints from the seismic data as explicit as possible in the posterior distribution. From a technical perspective, however, this may not have been the best choice. Narrower Gaussian priors or similar bell-shaped distributions may have accelerated the convergence of the Neighbourhood Algorithm. While the choice of a bell-shaped prior for the purpose of improved convergence would have been computationally beneficial, it would also have violated the fundamentals of Bayesian philosophy that do not allow to make choices on the basis of technical or convenience arguments (Scales & Snieder 1997).

To some extent, the spatial filtering of the test models reduces the originally constant priors to more Gaussian-type distributions. The strength of this modification is inversely proportional to the volume of a specific basis function, and it acts to equilibrate in a natural way the effective number of degrees of freedom in relation to the volume of a basis function. It follows that the effective dimension

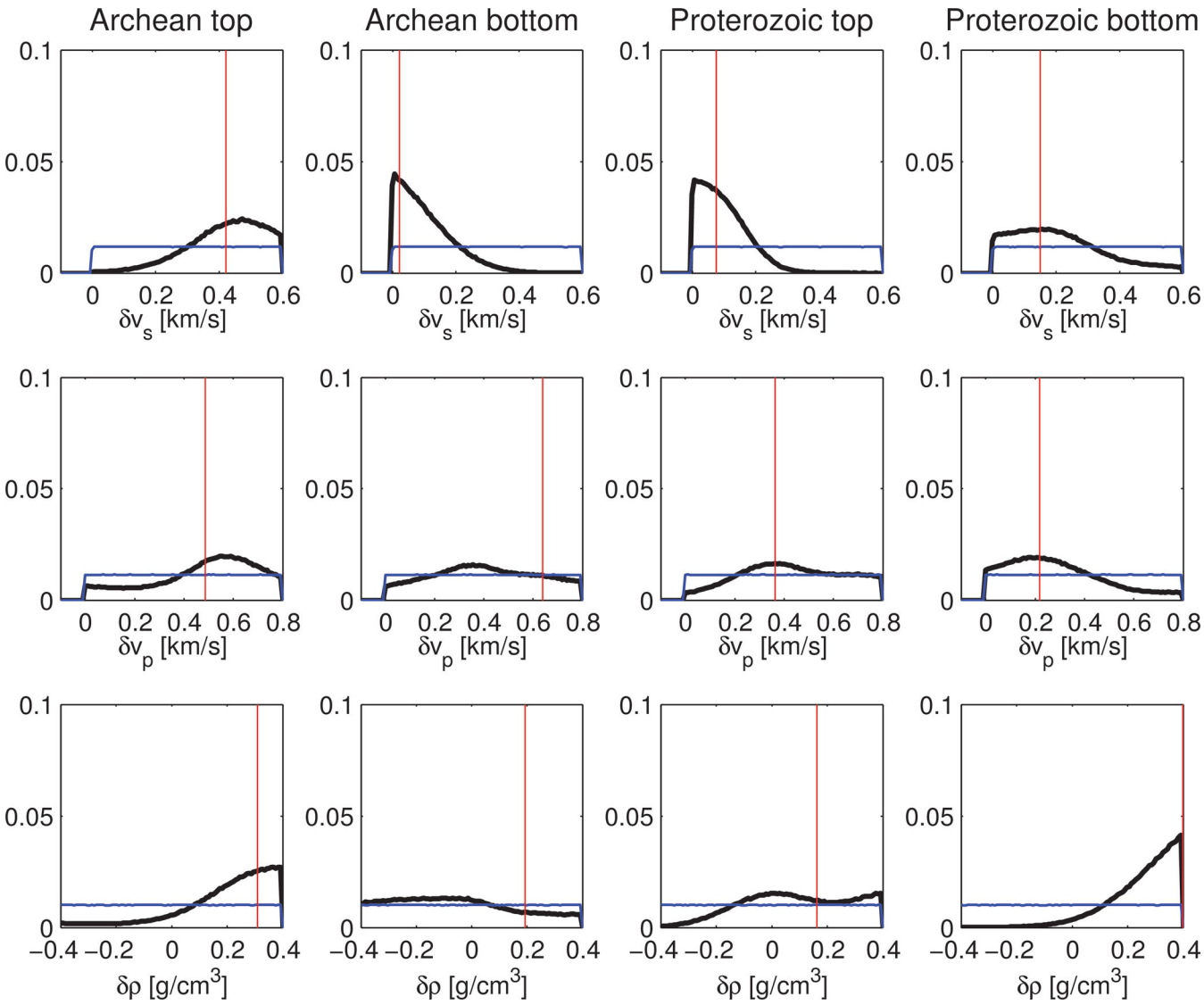

Figure 12. Prior (blue) and posterior (black) marginal distributions for the original 12 parameters, that is, without accounting for the spatial filtering used in the construction of test models for the same noise level as in Fig. 10.

of the parameter space is less than 12 because of the correlations introduced by the spatial filtering.

6.2 Noise model

Noise occurs in seismological waveform data due to several distinct effects, including ambient seismic noise, unexplained signal due to unmodelled 3-D structure, a simplified model parametrization and neglected or inaccurate physics (e.g. Gouveia & Scales 1998). In our particular application, we assume that data noise—in the sense of a quasi-randomly propagating wave field—does not play a significant role since we only selected seismograms where noise is essentially absent. Furthermore seismic noise power spectra typically show a pronounced minimum between 50 and 200 s periods (Peterson 1993). As a consequence, our noise is by far dominated by unmodeled 3-D heterogeneity, neglected anisotropy, 3-D variations of Q, and incorrect source characteristics.

Since these effects are extremely difficult to assess quantitatively, we prefer a simplified noise model over a description in terms of full noise covariance matrices that account for spatio-temporal correlations. While it is hard, but possible to estimate spatio-temporal correlations of ambient noise in low-frequency bands, the covariance structure of the other sources of noise is plainly unknown and would require an unrealistic effort.

We thus conclude that while technically we are dealing with correlated ambient noise, the part of the misfit that is due to ambient noise is small compared to other effects mentioned above. We have to note, however, that as with any other kind of prior information, the results have to be seen in relation to the chosen noise model and are expected to be affected by the particular choice. We stress that the choice of an appropriate noise model is a very important one in every Bayesian analysis. A promising and more general approach might be a transdimensional inversion (e.g. Bodin *et al.* 2012a,b), which treats data- and parametrization-error in a unified framework.

6.3 Tractable number of model parameters

Our approach to probabilistic tomography is based on a severe model space reduction that we achieved with the help of tectonic regionalization. In retrospect, however, 12 dimensions may already

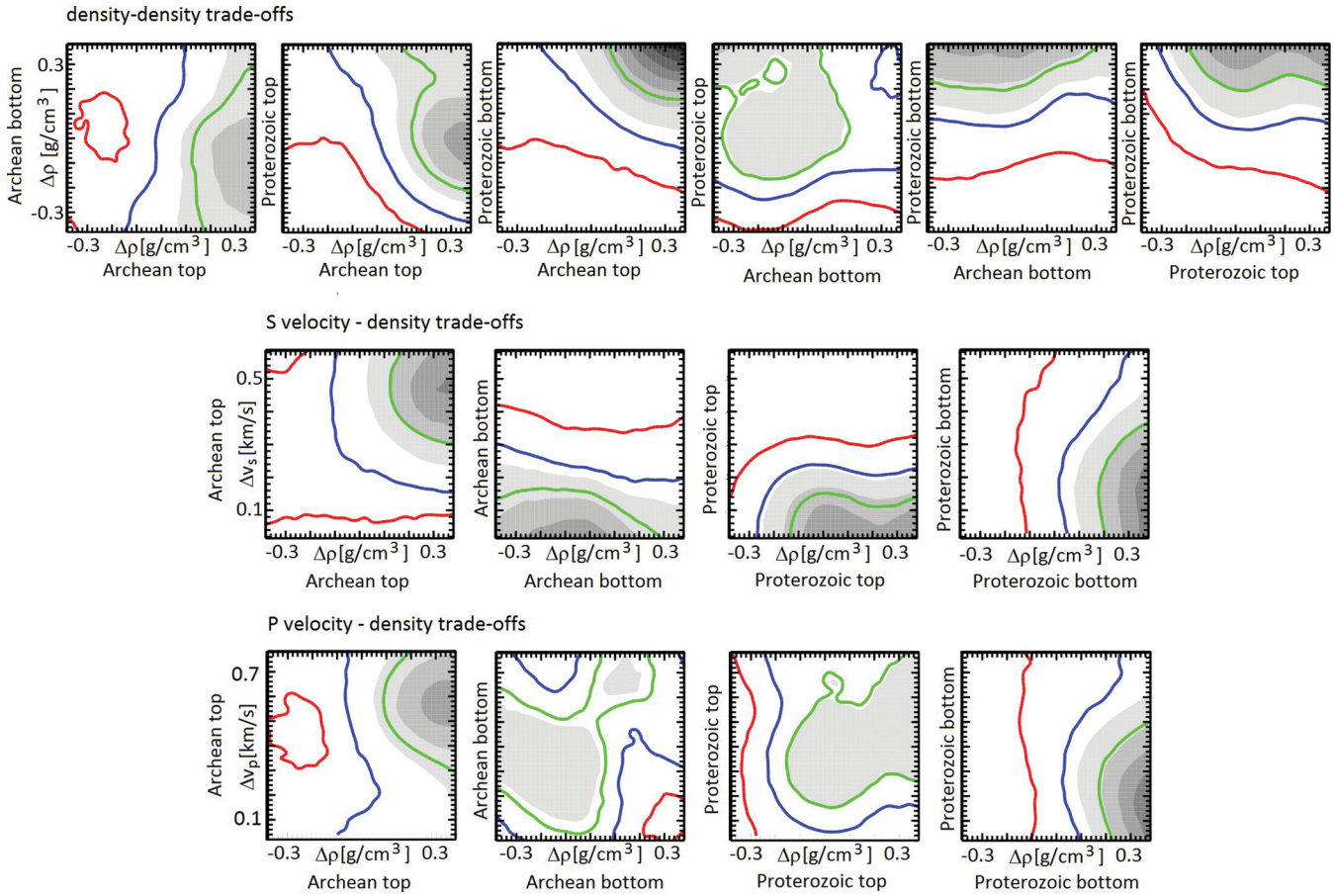

Figure 13. 2-D posterior marginals showing density-density as well as a collection of velocity–density trade-offs. Darker regions correspond to higher probability densities. There are no significant 2-D trade-offs that permit a reduction of density variations to more plausible values in the Archean top and Proterozoic bottom layers without increasing the misfit significantly.

be too much when the topology of the misfit surface is complicated and significantly non-Gaussian. This statement seems to be fundamental and not specific to our application. Sampling algorithms in general have difficulties to detect comparatively small subvolumes with low-misfit models. This problem becomes increasingly severe with increasing dimension because the probability of drawing samples from the less plausible boundary regions of the model rapidly approaches 1. It therefore becomes nearly impossible to sample the interior regions of the model space where highly plausible models are often located (e.g. Backus 1988; Curtis & Lomax 2001; Jackson & Sambridge 2005). Alternatives to the Neighbourhood Algorithm such as Hybrid Monte Carlo techniques (e.g. Duane *et al.* 1987) or Neural Networks (e.g. Devilee *et al.* 1999; Meier *et al.* 2007b,a) may help to attenuate this problem, but their potential in the context of seismic tomography still remains to be fully explored.

Regardless of sampling issues, the interpretation of a high-dimensional posterior is a major—and also very general—challenge. Most of our analysis is based on one- or two-dimensional condensations of the posterior that are unable to detect potentially important subtleties that involve more than two parameters. The transition to higher-dimensional probabilistic full waveform inversion therefore not only relies on an increase of computational power but also on the resolution of much more fundamental issues related to the sampling of complicated posteriors and their analysis.

6.4 Nongravitational constraints on density

One of the primary goals of this study was the analysis of constraints on density that do not arise from the very long-period gravitational restoring force (e.g. Ishii & Tromp 2001; Resovsky & Trampert 2003; Trampert *et al.* 2004) but from elastic effects. From a purely seismological perspective, our data seem to prefer high-density models of the central and western Australian lithosphere (up to +6 per cent). However, the inconsistence of this result with independent constraints from geodynamics and mineral physics (e.g. Jordan 1975; James *et al.* 2004; Reigber *et al.* 2007) calls for caution. It is most likely due to a combination of two closely related effects: First, there may exist trade-offs between density and other parameters that cause the high-density models to be insignificant. These trade-offs are unlikely to take the form of broad and simplistic two-parameter compensations, for example, between density and *S* velocity, as they would be visible in the 2-D marginals of Fig. 13. Second, the shape of the misfit surface in density subspace is too complicated to be fully captured by sampling with a comparatively small number of samples. One explanation for the nearly exponential 1-D marginals in Fig. 12 is that the most plausible density models are located in a small subvolume that can hardly be discovered by one of the samples. The Neighbourhood Algorithm may therefore converge to a much broader subvolume of high-density models that are less plausible while still explaining the data better than the vast majority of intermediate- or low-density models.

Concerning density, an important finding at this point is that 3-D density variations do have a significant effect on seismic waveforms at intermediate periods between 60 and 200 s. This effect, however, can be misleading because the basin of attraction of the global optimum does not seem to be particularly broad—despite complete 3-D modelling and full waveform misfits. It follows immediately that a deterministic full waveform inversion for density heterogeneities requires a very good initial model, which was also indirectly suggested by Jeong *et al.* (2012). This statement must, of course, be seen in the context of the comparatively long periods used in our study. At shorter periods where seismograms are more strongly affected by the scattering properties of the Earth, backward-scattered waves from density heterogeneities (e.g. Wu & Aki 1985; Tarantola 1986) may yield additional constraints, at least when full waveform misfits are used.

6.5 Geological implications

The posterior marginals in the first row of Figs 10–12 reveal that strongly elevated S velocities down to 230 km depth in the Archean lithosphere of western Australia are well constrained, and most likely to range between +3 per cent and +5 per cent on ∼1000 km length scales. These values are significantly lower than the localized +12 per cent S velocity variations in the model of Fichtner *et al.* (2010a) that would translate to temperatures around 0 °C in the case of a purely thermal effect (e.g. Cammarano *et al.* 2003; Priestley & McKenzie 2006, S. Goes, personal communication). This suggests that a compositional contribution to S velocity heterogeneities is strictly required only locally, that is, on length scales below ∼500 km.

In the shallower part of the model, to depths of ∼150 km, Proterozoic central Australia is characterized by elevated S velocities that are well constrained to $+2 \pm 1$ per cent. It follows that lower than average S velocities (e.g. Fishwick & Reading 2008) are also likely to be a localized feature that has little effect on the large-scale characteristics of the central Australian lithosphere.

7 CONCLUSIONS

We presented a study to investigate the feasibility of 3-D probabilistic full waveform inversion. Our approach is based on spectral-element simulations of seismic wave propagation combined with a quasi-random exploration of the model space using the Neighbourhood Algorithm. As data we used seismograms in the period range from 60 to 200 s, recorded at mostly permanent stations in Australia. To reduce the size of the model space, we parametrized the Australian continent in terms of large-scale basis functions that result from a tectonic regionalization.

Our results indicate that S velocities in the upper 150 km are particularly well constrained and positive, in accord with previous deterministic tomographies. Peak S velocity heterogeneities in the Archean lithosphere range around 4 per cent over ∼1000 km length scales, suggesting that extreme values of +12 per cent (Fichtner *et al.* 2010a) are indeed localized features. The maximum likelihood model reveals consistently elevated P velocities. While consistent with body wave studies, they are less well constrained by our data, because the corresponding posterior marginals are less pronounced and become effectively flat, when the noise level is increased. This provides a remarkable example of a maximum likelihood model that appears plausible but may be practically irrelevant, and underlines the need of a proper uncertainty analysis.

Our data are notably affected by 3-D density variations. The effect, however, appears to be misleading. Both the maximum-likelihood model and the posterior probability densities strongly prefer unrealistically large positive density variations that are inconsistent with the absence of large-scale geoid anomalies, the long-term gravitational stability of central and western Australia, and densities of plausible lithospheric compositions. This suggests that highly probable and less extreme density models may be hidden in small and hardly detectable subvolumes of the 12-D model space. The basin of attraction of the global optimum for density appears to be comparatively narrow, and the failure to detect this basin cannot be reflected in any convergence measure of the Monte Carlo exploration. As in deterministic inversions, a broad basin of attraction seems to be a pre-requisite for a successful inversion. It follows that deterministic full waveform inversions for density may require particularly accurate initial models.

From a methodological perspective a transition to significantly higher dimensions seems difficult at present. Available computing power clearly imposes very concrete restrictions. However, even with increasing computational resources and the use of adaptive sampling techniques, the largest obstacle remains to be our inability to efficiently map small high-dimensional subvolumes with high probability.

ACKNOWLEDGMENTS

We acknowledge support from the Bavarian Ministry of Sciences (KONWIHR Project) and the computational resources provided by the Leibniz Rechenzentrum Munich (project h019z). We also benefited from the Marie-Curie funded Initial Training Network QUEST. Andreas Fichtner was funded by The Netherlands Research Center for Integrated Solid Earth Sciences under project number ISES-MD.5. Paul Käufl was partly funded by the Dutch National Research Grant under the grant number ALW Top-subsidy 854.10.002. Discussions with Jeannot Trampert, Malcolm Sambridge, Brian Kennett, Jeroen Tromp, Carène Larmat and Monica Maceira, as well as the careful and constructive reviews of Thomas Bodin and Carl Tape helped us to improve the manuscript.

REFERENCES

An, M., 2012. A simple method for determining the spatial resolution of a general inverse problem, *Geophys. J. Int.,* **191,** 849–864.

Backus, G.E., 1988. Bayesian inference in geomagnetism, *Geophys. J.,* **92,** 125–142.

Bodin, T., Sambridge, M., Tkalčić, H., Arroucau, P., Gallagher, K. & Rawlinson, N., 2012a. Transdimensional inversion of receiver functions and surface wave dispersion, *J. geophys. Res.,* **117,** B02301.

Bodin, T., Sambridge, M., Rawlinson, N. & Arroucau, P., 2012b. Transdimensional tomography with unknown data noise, *Geophys. J. Int.,* **189,** 1536–1556.

Bozdağ, E., Trampert, J. & Tromp, J., 2011. Misfit functions for full waveform inversion based on instantaneous phase and envelope measurements, *Geophys. J. Int.,* **185,** 845–870.

Brossier, R., Operto, S. & Virieux, J., 2010. Which data residual norm for robust elastic frequency-domain full waveform inversion? *Geophysics,* **75,** R37–R46.

Cammarano, F., Goes, S., Vacher, P. & Giardini, D., 2003. Inferring upper-mantle temperatures from seismic velocities, *Phys. Earth planet. Int.,* **138,** 197–222.

Chen, P., Zhao, L. & Jordan, T.H., 2007. Full 3D tomography for the crustal structure of the Los Angeles region, *Bull. seism. Soc. Am.,* **97,** 1094–1120.

Crase, E., Pica, A., Noble, M., McDonald, J. & Tarantola, A., 1990. Robust elastic nonlinear waveform inversion—application to real data, *Geophysics,* **55,** 527–538.

Curtis, A. & Lomax, A., 2001. Prior information, sampling distributions, and the curse of dimensionality, *Geophysics,* **66,** 372–378.

de Wit, R. W.L., Trampert, J. & van der Hilst, R.D., 2012. Toward quantifying uncertainty in travel time tomography using the null-space shuttle, *J. geophys. Res.,* **117,** B03301.

Deal, M.M. & Nolet, G., 1996. Nullspace shuttles, *Geophys. J. Int.,* **124,** 372–380.

Debayle, E. & Kennett, B.L.N., 2000. The Australian continental upper mantle: Structure and deformation inferred from surface waves, *J. geophys. Res.,* **105,** 25 423–25 450.

Devilee, R. J.R., Curtis, A. & Roy-Chowdhury, K., 1999. An efficient, probabilistic neural network approach to solving inverse problems: inverting surface wave velocities for Eurasian crustal thickness, *J. geophys. Res.,* **104,** 28 841–28 857.

Duane, S., Kennedy, A.D., Pendleton, B.J. & Roweth, D., 1987. Hybrid Monte Carlo, *Phys. Lett. B,* **195,** 216–222.

Dziewonski, A.M. & Anderson, D.L., 1981. Preliminary reference Earth model, *Phys. Earth planet. Inter.,* **25,** 297–356.

Dziewonski, A.M. & Steim, J.M., 1982. Dispersion and attenuation of mantle waves through waveform inversion, *Geophys. J. Int.,* **70,** 503–527.

Fichtner, A., de Wit, M. & van Bergen, M., 2010a. Subduction of continental lithosphere in the banda sea region: combining evidence from full waveform tomography and isotope ratios, *Earth planet. Sci. Lett.,* **297,** 405–412.

Fichtner, A., Fishwick, S., Yoshizawa, K. & Kennett, B.L.N., 2012. Optimal spherical spline filters for the analysis and comparison of regional-scale tomographic models, *Phys. Earth planet. Int.,* **190-191,** 44–50.

Fichtner, A., Kennett, B.L.N., Igel, H. & Bunge, H.-P., 2008. Theoretical background for continental- and global-scale full-waveform inversion in the time-frequency domain, *Geophys. J. Int.,* **175,** 665–685.

Fichtner, A., Kennett, B.L.N., Igel, H. & Bunge, H.-P., 2010b. Full waveform tomography for radially anisotropic structure: new insights into present and past states of the Australasian upper mantle, *Earth planet. Sci. Lett.,* **290,** 270–280.

Fichtner, A. & Trampert, J., 2011a. Hessian kernels of seismic data functionals based upon adjoint techniques, *Geophys. J. Int.,* **185,** 775–798.

Fichtner, A. & Trampert, J., 2011b. Resolution analysis in full waveform inversion, *Geophys. J. Int.,* **187,** 1604–1624.

Fishwick, S., Kennett, B. L.N. & Reading, A.M., 2005. Contrasts in lithospheric structure within the Australian craton—insights from surface wave tomography, *Earth planet. Sci. Lett.,* **231,** 163–176.

Fishwick, S. & Reading, A.M., 2008. Anomalous lithosphere beneath the Proterozoic of western and central Australia: a record of continental collision and intraplate deformation? *Precambrian Res.,* **166,** 111–121.

Freeden, W., Gervens, T. & Schreiner, M., 1998, *Constructive Approximation on the Sphere*. Oxford Science Publications, Clarendon Press, Oxford.

Gauthier, O., Virieux, J. & Tarantola, A., 1986. Two-dimensional nonlinear inversion of seismic waveforms: numerical results, *Geophysics,* **51,** 1387–1403.

Gee, L.S. & Jordan, T.H., 1992. Generalized seismological data functionals, *Geophys. J. Int.,* **111,** 363–390.

Gouveia, W.P. & Scales, J.a., 1998. Bayesian seismic waveform inversion: parameter estimation and uncertainty analysis, *J. geophys. Res.* **103**(B2), 2759–2779.

Handler, M., Bennett, V.C. & Esat, T.M., 1997. The persistence of off-cratonic lithospheric mantle: Os isotopic systematics of variably metasomatised southeast Australian xenoliths, *Earth planet. Sci. Lett.,* **151,** 61–75.

Horbach, A., 2008, Analysis of the cosmic microwave background observed by WMAP, *Diploma thesis,* TU Kaiserslautern.

Ishii, M. & Tromp, J., 2001. Even-degree lateral variations in the Earth's mantle constrained by free oscillations and the free-air gravity anomaly, *Geophys. J. Int.,* **145,** 77–96.

Jackson, A. & Sambridge, M., 2005. Softening a hard quadratic bound to a prior pdf—an example from geomagnetism, Bayesian Inference and Maximum Entropy Methods in Science and Engineering Book Series, *AIP Conf. Proc.,* **803,** 499–506.

James, D.E., Boyd, F.R., Schutt, D., Bell, D.R. & Carlson, R.W., 2004. Xenolith constraints on seismic velocities in the upper mantle beneath Africa, *Geochem. Geophys. Geosys.,* **5,** doi:10.1029/2003GC000551.

Jaynes, E.T., 2003, *Probability Theory—The Logic of Science*. Cambridge University Press, Cambridge, UK.

Jeong, W., Lee, H.-Y. & Min, D.-J., 2012. Full waveform inversion strategy for density in the frequency domain, *Geophys. J. Int.,* **188,** 1221–1242.

Jordan, T.H., 1975. The continental tectosphere, *Rev. Geophys. Space Phys.,* **13,** 1–12.

Kaiho, Y. & Kennett, B. L.N., 2000. Three-dimensional seismic structure beneath the Australasian region from refracted wave observations, *Geophys. J. Int.,* **142,** 651–668.

Kanamori, H., 1970. Velocity and Q of mantle waves, *Phys. Earth planet. Int.,* **2,** 259–275.

Kennett, B., Fichtner, A., Fishwick, S. & Yoshizawa, K., 2013. Australian seismological reference model (AuSREM): mantle component, *Geophys. J. Int.,* in press.

Köhn, D., Kurzmann, A., Przebindowska, A., de Nil, D. & Bohlen, T., 2010. 2D elastic full waveform tomography of synthetic marine reflection seismic data, *DGG Mitteilungen,* **1/2010,** 23–27.

Lekic, V. & Romanowicz, B., 2011. Inferring upper mantle structure by full waveform tomography using the spectral element method, *Geophys. J. Int.,* **185,** 799–831.

Lévêque, J.J., Rivera, L. & Wittlinger, G., 1993. On the use of the checkerboard test to assess the resolution of tomographic inversions, *Geophys. J. Int.,* **115,** 313–318.

Meier, U., Curtis, A. & Trampert, J., 2007a. Fully nonlinear inversion of fundamental mode surface waves for a global crustal model, *Geophys. Res. Lett.,* **34,** doi:10.1029/2007GL030989.

Meier, U., Curtis, A. & Trampert, J., 2007b. Global crustal thickness from neural network inversion of surface wave data, *Geophys. J. Int.,* **169,** 706–722.

Myers, J.S., Shaw, R.D. & Tyler, I.M., 1996. Tectonic evolution of Proterozoic Australia, *Tectonics,* **15,** 1431–1446.

Oeser, J., Bunge, H.-P. & Mohr, M., 2006. Cluster design in the Earth sciences: TETHYS, *Lect. Notes Comput. Sci.,* **4208,** 31–40.

Peterson, J., 1993. Observations and modelling of seismic background noise, USGS Open-file report, 93–322.

Priestley, K. & McKenzie, D., 2006. The thermal structure of the lithosphere from shear velocities, *Earth planet. Sci. Lett.,* **244,** 285–301.

Reigber, C. *et al.*, 2007. A high-resolution global gravity field model combining CHAMP and GRACE satellite mission and surface data: EIGEN-CG01C, GFZ Scientific Technical Report, 06/07, 12 pp.

Resovsky, J. & Trampert, J., 2003. Using probabilistic seismic tomography to test mantle velocity-density relationships, *Earth planet. Sci. Lett.,* **215,** 121–134.

Rickers, F., Fichtner, A. & Trampert, J., 2012. Imaging mantle plumes with instantaneous phase measurements of diffracted waves, *Geophys. J. Int.,* **190,** 650–664.

Sambridge, M., 1999a. Geophysical inversion with the Neighbourhood Algorithm—I. Searching a parameter space, *Geophys. J. Int.,* **138,** 479–494.

Sambridge, M., 1999b. Geophysical inversion with the Neighbourhood Algorithm—II. Appraising the ensemble, *Geophys. J. Int.,* **138,** 727–746.

Scales, J.A. & Snieder, R., 1997. To Bayes or not to Bayes? *Geophysics,* **62,** 1045–1046.

Simons, F.J., van der Hilst, R.D., Montagner, J.-P. & Zielhuis, A., 2002. Multimode Rayleigh wave inversion for heterogeneity and azimuthal anisotropy of the Australian upper mantle, *Geophys. J. Int.,* **151,** 738–754.

Takeuchi, H. & Saito, M., 1972. Seismic surface waves, *Methods Comput. Phys.,* **11,** 217–295.

Tape, C., Liu, Q., Maggi, A. & Tromp, J., 2009. Adjoint tomography of the southern California crust, *Science,* **325,** 988–992.

Tarantola, A., 1986. A strategy for nonlinear elastic inversion of seismic reflection data, *Geophysics,* **51,** 1893–1903.
Tarantola, A., 2005, *Inverse Problem Theory and Methods for Model Parameter Estimation,* 2nd edn, Society for Industrial and Applied Mathematics, Philadelphia.
Trampert, J., Deschamps, F., Resovsky, J. & Yuen, D., 2004. Probabilistic tomography maps chemical heterogeneities throughout the lower mantle, *Science,* **306,** 853–856.
Trampert, J., Fichtner, A. & Ritsema, J., 2012. Resolution tests revisited: the power of random numbers, *Geophys. J. Int.,* **192,** 676–680.
Wellman, P., 1998. Mapping of geophysical domains in the Australian continental crust using gravity and magnetic anomalies, in *Structure and Evolution of the Australian Continent,* eds Braun, J., Dooley, J., Goleby, B., van der Hilst, R. & Klootrwijk, C., pp. 59–71, AGU Geodynamics Series 26.
Wu, R. & Aki, K., 1985. Scattering characteristics of elastic waves by an elastic heterogeneity, *Geophysics,* **50,** 582–595.
Yoshizawa, K. & Kennett, B. L.N., 2004. Multimode surface wave tomography for the Australian region using a three-stage approach incorporating finite frequency effects, *J. geophys. Res.,* **109,** doi:10.1029/2002JB002254.
Zielhuis, A. & van der Hilst, R.D., 1996. Upper-mantle shear velocity beneath eastern Australia from inversion of waveforms from SKIPPY portable arrays, *Geophys. J. Int.,* **127,** 1–16.

APPENDIX A: SPATIAL FILTERING OF REGIONAL EARTH MODELS

In the following paragraphs we describe the spatial filtering of tomographic models that is intended to avoid the occurrence of unrealistic guided and reflected waves from the sharp boundaries of the basis functions. More technical details can be found in Fichtner *et al.* (2012).

A1 Radial filtering

Filtering in the radial direction is implemented as a radial convolution of a model parameter $m(\mathbf{x}) = m(r\,\mathbf{e}_r)$ and a depth-dependent Gaussian $g(r, \xi)$:

$$(F_r * m)(\mathbf{x}) := \int_{r=0}^{R} m(\xi\,\mathbf{e}_r)\, g(r, \xi)\, \mathrm{d}\xi$$

$$\text{with} \quad g(r, \xi) := \frac{1}{\sigma(r)\sqrt{\pi}} \mathrm{e}^{-(r-\xi)^2/\sigma^2(r)}\,, \tag{A1}$$

The symbols $\mathbf{e}_r$ and R denote the unit vector in radial direction and the radius of the Earth. We require that the width $\sigma(r)$ of the Gaussian be monotonically increasing with increasing depth and equal to zero at the surface $r = R$. This ensures that more details are preserved at shallow depth and that filtering artefacts near the surface are avoided. Empirically we found that $\sigma(r)$ of the form

$$\sigma(r) = \sigma_0 \left[1 - \, d^{-(R-r)^2/\sigma_0^2}\right], \tag{A2}$$

with $\sigma_0 = 40$ km yields acceptable results.

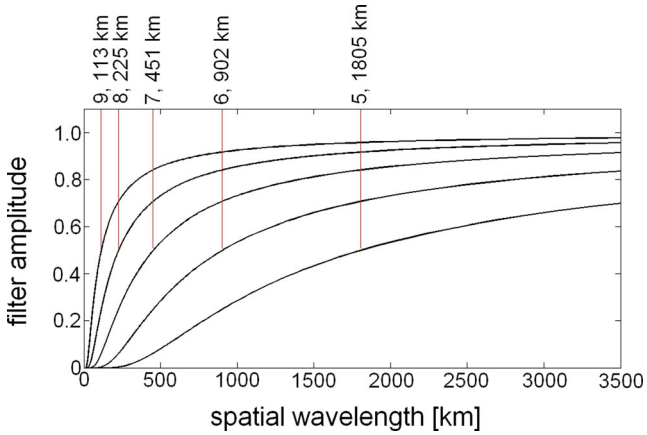

Figure A1. Filter characteristics of the Abel-Poisson scaling functions for different scales j, ranging from 5 to 9. The curves indicate the factors by which features of a given spatial wavelength are damped. The red lines mark the corner wavelengths of the different filters, defined as the wavelength where the filter characteristics reach the value 0.5. Note the optical illusion.

A2 Horizontal direction

The filtering operation in horizontal direction is a spherical convolution of the model parameter $m(\mathbf{x})$ with a scaling function $\phi_j \in L_2([-1, 1])$ of scale $j \in \mathbb{N}$

$$(F_h * m)(\mathbf{x}) = \int_{\partial G \subset \Omega} \phi_j(\boldsymbol{\xi} \cdot \mathbf{x}) m(\boldsymbol{\xi})\, d^2\boldsymbol{\xi}\,. \tag{A3}$$

The integral is over the part ∂G of the unit sphere Ω where our model is located. For ϕ_j we choose the Abel–Poisson scaling function

$$\phi_j(x) = \frac{1}{4\pi} \frac{1 - h^2}{(1 + h^2 - 2hx)^{3/2}}\,, \quad h = e^{-2^{-j}}\,, \tag{A4}$$

The spherical convolution acts as a lowpass filter, meaning that shorter wavelengths are suppressed more than longer wavelengths. Fig. A1 illustrates the filter characteristics as a function of the scale j. For a more detailed account of spatial filtering on the sphere, the reader is referred to Freeden *et al.* (1998) and Horbach (2008). The complete spatial filter F is then defined through the application of both F_r and F_h to an Earth model. Eq. (1b) may thus be written as

$$m(\mathbf{x}) = (F * \tilde{m})(\mathbf{x}) = (F_r * F_h * \tilde{m})(\mathbf{x})\,. \tag{A5}$$